# Observation of the surface horizontal thermohaline variability at mesoscale to submesoscale in the north-eastern subtropical Atlantic Ocean

Nicolas N. Kolodziejczyk, Gilles Reverdin, Jacqueline Boutin, Olga Hernandez

AGU PUBLICATIONS

JGR

Journal of Geophysical Research: Oceans

RESEARCH ARTICLE

10.1002/2014JC010455

**Key Points:**
- In the eastern subtropics, density compensation at all scales in winter
- thermohaline spectra in $k^{-3}$ at submesoscale in winter
- Thermohaline spectra flatter in summer

**Correspondence to:**
N. Kolodziejczyk,
nicolas.kolodziejczyk@gmail.com

**Citation:**
Kolodziejczyk, N., G. Reverdin, J. Boutin, and O. Hernandez (2015), Observation of the surface horizontal thermohaline variability at mesoscale to submesoscale in the north-eastern subtropical Atlantic Ocean, *J. Geophys. Res. Oceans*, *120*, 2588–2600, doi:10.1002/2014JC010455.

Received 17 SEP 2014
Accepted 13 MAR 2015
Accepted article online 18 MAR 2015
Published online 2 APR 2015
Corrected 22 May 2015

This article was corrected on 22 MAY 2015. See the end of the full text for details.



# Observation of the surface horizontal thermohaline variability at mesoscale to submesoscale in the north-eastern subtropical Atlantic Ocean

**Nicolas Kolodziejczyk[1], Gilles Reverdin[1], Jacqueline Boutin[1], and Olga Hernandez[1]**

[1]Sorbonne Universités (UPMC, Univ Paris 06)-CNRS-IRD-MNHN, LOCEAN Laboratory, Paris, France

**Abstract** The seasonal variability of the surface horizontal thermohaline structure is investigated in the north-eastern Atlantic Surface Salinity Maximum (SSM) at length scales from five to hundreds of kilometers, i.e., at submesoscale to mesoscale. The near-surface temperature and salinity data from merchant ship thermosalinograph (TSG) transects across the Atlantic are used to compute the horizontal temperature, salinity and density fluctuations, and the density ratio. During late winter in the north-eastern SSM, thermohaline compensation is observed for wavelengths from 5 km to more than 200 km; in spite of large and sharp surface thermohaline fronts, a weak density surface horizontal gradient is observed. Temperature and salinity exhibit an energetic spectra in $k^{-2}$ slope scale between 20–100 km scale and a steeper slope at shorter wavelengths, while density spectra exhibit lower energy level with a clear $k^{-3}$ slope below 20 km, consistent with interior quasigeostrophic turbulence. During summer in the north-eastern SSM, salinity and temperature gradients are no longer compensated due to strong atmospheric heating of the upper ocean. In comparison with winter, the surface density spectrum is enhanced with a flatter slope between $k^{-2}$ and $k^{-1}$ between 5 and 20 km.

## 1. Introduction

The properties of the mixed layer horizontal thermohaline structures, i.e., the temperature and salinity contrasts, have been shown to vary as a function of location, season, and as a function of spatial scales. Within subtropical latitudes, at large scales, the temperature variability dominates the seasonal surface density changes through the seasonal cycle of solar heat flux [*Johnson et al*., 2012]; thus, usually the buoyancy horizontal gradient is annually driven by temperature variability [*Stommel*, 1993]. In the tropics, high precipitations and river discharges produce strong and shallow vertical and horizontal gradients in the upper ocean [*Reverdin et al*., 2007; *Mignot et al*. 2012; *Tanguy et al*., 2010]. At mesoscale, the surface thermohaline structures are mainly driven by the baroclinic instability of the currents located at frontal regions, which are the main source of eddies in the world ocean. These oceanic mesoscale eddies (50–500 km) contribute to horizontal heat and salt contrasts and transports on a global scale [*Dong et al*., 2014]. The mesoscale fronts contribute to the cascade of energy toward smaller scales, named the submesoscales, so that the mixing ultimately diffuses the horizontal density field and reduces the horizontal density gradient [*Samelson and Paulson*, 1988, *Young*, 1994; *Rudnick and Martin*, 2002; *Klein et al*., 2008; *Callies and Ferrari*, 2013].

The surface density structure at the mesoscale or submesoscale can reflect the dominant processes of potential energy conversion in the upper ocean. First, surface quasigeostrophic (SQG) turbulence theory suggested a $k^{-5/3}$ slope for the surface potential energy spectra, while the interior quasigeostrophic theory predicts a $k^{-3}$ slope [*Charney*, 1971; *Callies and Ferrari*, 2013]. If one includes the ageostrophic part of the velocity and buoyancy, the slope of the potential energy will behave more as $k^{-2}$ [*Capet et al*., 2008]. Ageostrophic processes that can flatten the spectra at smaller scales are: Ekman flows, mixed layer turbulence, near inertial oscillation, internal tides, and the frontal circulation [*Callies and Ferrari*, 2013]. In the surface mixed layer, horizontal density fronts slump under gravity, which competes with the vertical shear and mixing thus induced by thermal wind (due to surface horizontal density gradient) and surface forcing. Vertical mixing diffuses the horizontal density field and reduces the horizontal density gradient [*Young*, 1994; *Rudnick and Martin*, 2002]. The net results are that density fronts are diffused while the temperature and salinity

compensated fronts persist. Strong horizontal density gradient and vertical velocity shears are sources of baroclinic and mixed layer instabilities that play a major role in mixed layer restratification [e.g., *Haine and Marshall*, 1998; *Marshall and Scott*, 1999; *Ferrari and Paparella*, 2003; *Boccaletti et al*., 2007; *Fox-Kemper et al*., 2008; *Fox-Kemper and Ferrari*, 2008].

The surface density gradient is primarily driven by the horizontal thermal and haline contrasts. To the first-order, the density fluctuation can be written as a linear combination of the temperature and salinity fluctuations:

$$\frac{\Delta\rho}{\rho_0} = \beta\Delta S - \alpha\Delta\theta \tag{1}$$

where $\alpha$ and $\beta$ are the constant coefficients of thermal expansion and of haline contraction of sea water. $\rho_0$=1025 kg m$^{-3}$ is the reference density [e.g., *Yeager and Large*, 2007]. $\Delta\rho$, $\Delta\theta$, and $\Delta S$ are the horizontal differentiations of potential density, potential temperature, and salinity of sea water. In this context, a measure of the relative effect of temperature and salinity on density is given by the density ratio:

$$R = \frac{\alpha\Delta\theta}{\beta\Delta S} \tag{2}$$

In the horizontal plane, the density ratio $R$=1 indicates that the horizontal gradient of temperature and salinity have opposite effects on density gradient, canceling and compensating each other. In this case, the thermohaline front could be very sharp while the density gradient remains weak. Thus, it plays a weak dynamical role. A density ratio $|R|>1$ indicates that the temperature gradient has a dominant effect on the density gradient, while a density ratio of $|R|<1$ corresponds to a dominant effect of the salinity gradient. The sign of the density ratio $R$ indicates whether the thermohaline gradients are in the same sense, thus have a compensating effect ($R>0$) or in opposite sense, thus have a constructive effect ($R<0$).

At midlatitudes, between 20° and 50°N in the three oceanic basins, *Stommel* [1993] noted that the density ratio is on average approximately $R=2$ during winter in the respective hemispheres. However, for thermohaline fronts between 100 m and 100 km wavelength, historical and recent observations have established that the surface thermohaline structure is compensated in subtropical regions between about 25°–35°N [*Roden*, 1974; 1991; *Rudnick and Luyten*, 1996; *Rudnick and Ferrari*, 1999; *Ferrari and Rudnick*, 2000; *Rudnick and Martin*, 2002]. $R$ greatly varies at larger scales (∼300–500 km) as a function of location and season as suggested in a recent global study of the horizontal near surface Turner angle computed from Argo autonomous floats [*Johnson et al*., 2012]. Unfortunately, the Argo array poorly samples some areas of main interest and the resolution of the Argo network (>300 km) is too coarse to resolve mesoscale to submesoscale horizontal thermohaline structures.

The recently launched Soil Moisture and Ocean Salinity (SMOS) satellite mission now allows to significantly improve the sampling of SSS observations [e.g., *Boutin et al*., 2004; *Font et al*., 2010; *Reul et al*. 2012, 2013]. For instance, in the subtropical North Atlantic Salinity maximum region (a region not affected by radio frequency interferences, far from the coast), after mean large scale bias correction, monthly 100 × 100 km$^2$ averaged SSS present a Root Mean Square Error (RMSE) of about 0.15 pss (Practical Salinity Scale PSS-78) compared to in situ measurements [*Hernandez et al*., 2014]. This gain of resolution in SSS products together with SST maps from satellite measurements allowed *Kolodziejczyk et al*. [2015] to compute the density ratio in the north-eastern subtropical Atlantic. During late boreal winter, they found that in the region of the Azores current temperature and salinity are mainly horizontally compensated at scales on the order of hundreds kilometers. However, this is not the case during boreal summer. Unfortunately, it is not possible to investigate the relative contribution of thermohaline varaibility at scales below 50 and 100 km with the SMOS SSS resolution (45 km).

In this study, the thermohaline horizontal surface structure and potential energy at mesoscale to submesoscale is investigated using high-resolution merchant ship thermosalinograph (TSG) data across the subtropical Atlantic Surface Salinity Maximum (SSM). This data are used in order to address the impact of surface mesoscale and submesoscale horizontal temperature and salinity variability on the distribution of horizontal density, i.e. the distribution of potential energy.

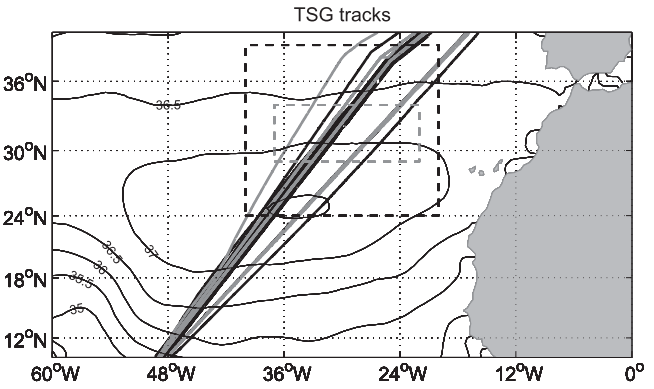


**Figure 1.** Colibri and Toucan tracks between 2002 and 2011 in the subtropical North Atlantic. The black (gray) tracks are taken during February–March (August–September). The black box is the box used for the PDF computation in section 4.1. The gray box is the box for which spectra are computed in section 4.2.

The paper is organized as follows. Data and Methods are presented in section 2. The spatial and wavelength distributions of the thermohaline structures over the North Atlantic SSM along the TSG transect carried out during March 2011 are described in section 3. This individual TSG transect was chosen in order to illustrate the method used in the paper and because it shows the typical horizontal thermohaline compensation of late boreal winter in the northeast SSM region. The seasonal variability of surface thermohaline structures and the temperature, salinity, and density spectra in the north-eastern part of the SSM are presented in section 4. Finally, results are discussed and summarized in section 5.

## 2. Data and Methods

### 2.1. Data

#### 2.1.1. Thermosalinograph T/S Data

High-resolution near-surface temperature and salinity data across the North Atlantic subtropical SSM are provided by thermosalinographs (TSG) mounted on the merchant vessels *Toucan* and *Colibri*. Temperature and salinity data were collected along transects from western Europe to northern South America since 1996 (Figure 1). These ships regularly cross the North Atlantic subtropical SSM between Europe and South America in about $\sim$ 10 days (at an average velocity of about 12–15 knots), and are thus able to capture SSS and SST features of the SSM over different seasons. The near surface sea water is pumped on the side of the immersed ship's hull at 5 m depth. Data are processed and flagged in order to remove noise caused, for example, by bubbles. The final horizontal resolution of this TSG product is of the order of 2.5 km. Post 2002 data are systematically post calibrated using scientific cruise CTD (conductivity-temperature-depth) data and collocated Argo float profile data at $\sim$ 5 m depth. The final error is typically on the order of 0.01 to 0.08 pss. Intercomparison with dropped-XBT profiles indicate that the TSG temperature is usually warmer by 0.2°C than T(XBT) at 3–5m, thus, this warm bias has been corrected within the TSG data (for further information see: http://www.legos.obs-mip.fr/observations/sss).

For the purpose of this study, only data with "Adjusted" and "Good" or "Probably Good" flagged data are used. However, for spectral analysis purpose, continuous space series are required. Thus, we systematically remove transects with too many data that are flagged as missing or poor. When missing values are isolated, they are replaced by linearly interpolated values. Finally, a visual control is performed on each transect in order to remove transects with remaining spurious/dubious spikes. All data that are deemed accurate are finally interpolated on a regular 1 km grid. This resulted in 8 and 11 transects being retained during late winter (February–March) and late summer (August–September). Temporally, data are spread between 2002 and 2011, with the bulk of the transects occurring after 2007 (Table 1).

#### 2.1.2. Argo Profiles

In this study, we also use individual Argo profiles in the north-eastern subtropical Atlantic between 2002 and 2012 as depicted in the gray box of Figure 1 (i.e., in the region of horizontal thermohaline compensation). The Argo profiles are provided by the Coriolis center (http://www.coriolis.eu.org/) with a quality control (QC) flag. We only use Argo data considered as good or probably good (QC 1 or 2 for Argo data). However, it appeared that a few erroneous data remained undetected ($<$ 1%). We thus perform an additional visual test to remove remaining erroneous profiles.

**Table 1.** TSG Data Collected on Merchant Ship between 2002 and 2011 in the Subtropical North Atlantic

| Dates | Voyage Code | Ship |
|---|---|---|
| 7–16 Feb. 2003 | DM FNAV 2003a | Toucan |
| 23 Feb. to 3 Mar. 2009 | DM FNHQ 2009b | Colibri |
| 25 Feb. to 5 Mar. 2007 | DM FNHQ 2007b | Colibri |
| 28 Feb. to 8 Mar. 2011 | DM FNHQ 2011b | Colibri |
| 8–17 Mar. 2009 | DM FNHQ 2011b | Colibri |
| 20–30 Mar. 2010 | DM FNAV 2010a | Toucan |
| 23 Mar. to 1 Apr. 2008 | DM FNHQ 2008b | Colibri |
| 28 Mar. to 6 Apr. 2010 | DM FNHQ 2010b | Colibri |
| 27 Jul. to 5 Aug. 2009 | DM FNAV 2007e | Toucan |
| 30 Jul. to 8 Aug. 2010 | DM FNHQ 2010d | Colibri |
| 07–15 Aug. 2011 | DM FNAV 2002d | Toucan |
| 10–18 Aug. 2009 | DM FNHQ 2009e | Colibri |
| 13–23 Aug. 2010 | DM FNHQ 2010d | Colibri |
| 27 Aug. to 05 Sep. 2009 | DM FNHQ 2009e | Colibri |
| 23 Aug. to 31 Aug. 2007 | DM FNAV 2007b | Toucan |
| 30 Aug. to 9 Sep. 2007 | DM FNHQ 2007g | Colibri |
| 12–21 Sep. 2009 | DM FNAV 2009 | Toucan |
| 16–25 Sep. 2007 | DM FNAV 2007c | Toucan |

## 2.2. Analysis

### 2.2.1. Wavelet Analysis

A quantitative description of the surface thermohaline structures is achieved by computing the density ratio over a wide range of horizontal scales. We suggest that the wavelet transform is a suitable analysis technique to quantify the density ratio, as it has the benefit of being both scale and location selective. In order to determine the temperature and salinity fluctuation as a function of scale and location, wavelet transforms were computed along $T$ and $S$ TSG ship tracks [*Ferrari and Rudnick*, 2000].

The wavelet transform is used to analyze spatial series that contain nonstationary power at many different wavelengths. Wavelets are derived by dilatation of the so-called mother wavelet. In the following analysis, we use the unscaled Morlet wavelet $\psi 0(\eta)$, consisting of a plane wave modulated by a Gaussian:

$$\psi_0(\eta) = \pi^{-1/4} e^{ik_0\eta} e^{-\eta^2/2} \tag{3}$$

where $k_0$ is a nondimensional wavelength and $\eta$ is a nondimensional space parameter [see *Torrence and Compo*, 1998]. The continuous wavelet transform of a discrete sequence of potential temperature $\theta(xn)$ and salinity $S(xn)$ is defined at the location $xn$ and for the scale $k0$ with a scaled and translated version of $\psi_0(\eta)$:

$$\Delta\theta(k, x_n) = \sum_{n'=0}^{N-1} \bar{\psi}\left(\frac{(n'-n)\delta x}{k}\right)\theta(x_{n'}) \tag{4.1}$$

$$\Delta S(k, x_n) = \sum_{n'=0}^{N-1} \bar{\psi}\left(\frac{(n'-n)\delta x}{k}\right) S(x_{n'}) \tag{4.2}$$

where the overbar indicates the complex conjugate. $\Delta\theta(k,x_n)$ and $\Delta S(k,x_n)$ are the complex wavelet coefficients of potential temperature and salinity, respectively. $\delta x$ is the data space resolution. By varying the wavelet scale $k$ and translating along the localized space index $n$, one describes both the amplitude as a function of the scale and how this amplitude varies in space. The subscript $0$ has been also dropped on $\psi$ in equation (4) to indicate that it is now scaled following the normalization of *Torrence and Compo*, [1998, their section 3b and 3c].

By multiplying the wavelet coefficients of $\theta(k,xn)$ and $S(k,xn)$ by the respective expansion and contraction coefficients $\alpha$ and $\beta$, the density fluctuation $\Delta\rho$ at the location $x_n$ and for the scale $k$ can be written as:

$$\frac{\Delta\rho}{\rho_0}(k, x_n) = \Re\{\beta S(k, x_n) - \alpha\theta(k, x_n)\} \tag{5}$$

where $\rho_0 = 1025$ kg m$^{-3}$. Note that, in the northern subtropical Atlantic, the surface coefficients $\alpha$ and $\beta$ are weakly dependent on location [*Tailleux et al.*, 2005]. Using constant instead of space-dependent coefficients along TSG tracks was found not to significantly change the results. Finally, the density ratio (2) at the location $x_n$ and for the scale $k$ can be written as:

$$R = \frac{\alpha\Delta\theta(k, x_n)}{\beta\Delta S(k, x_n)} \tag{6}$$

where the density ratio $R$ is complex. The phase $\Phi$ of the complex density ratio $R$ quantifies the coherence of $\Delta\theta$ and $\Delta S$ fluctuations. If the phase is $\Phi = 0°$ ($\Phi = 180°$), then the fluctuations of $\theta$ and $S$ at the location $x_n$

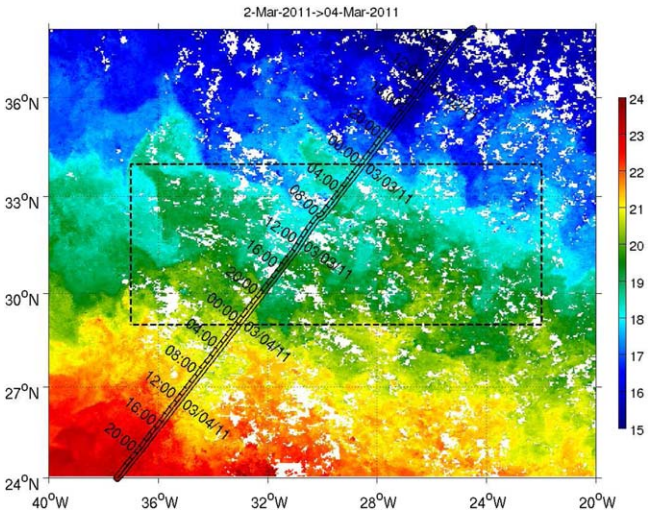


**Figure 2.** SST composite from Aqua and Terra MODIS daily 11 μm SST (in °C) between 2 and 4 March 2011 (downloaded from: http://oceancolor.gsfc.nasa.gov/). TSG track (solid black), SST (color along TSG track), and cruising dates (black ticks) for the March 2011 "Colibri" cruises. The dotted box define the north-south limits of the spectral analysis (corresponding to the gray box in Figure 1).

and for the scale $k$ are in the same direction (opposite), and act to reduce (strengthen) the density gradient. The magnitude of $R$ quantifies the relative strength of the fluctuations of $\theta$ and $S$.

### 2.2.2. Spectral Analysis

The selected TSG surface transects spanning 10 years of measurements are used to compute the wavenumber spectra of near surface temperature, salinity and density in the north-eastern SSM region of the subtropical North Atlantic between 29° and 34°N, in the region of the Azores Current/Front. This baroclinically unstable Current/Front is rich in mesoscale features and filamentations [*Alves and Colin de Verdière*, 1999; *Juliano and Alves*, 2007]. During late winter this front is well marked in SST, with associated eddies and filamentations clearly exhibiting a variety of length scales from 10 to 200 km, as illustrated from the Colibri transect on 2–4 March 2011 (colors along the transect in Figure 2).

In this region, 700 km-long complete transects were used, which correspond roughly to 1 day of data. For each transect, the spatial mean and linear trend are removed. Then, the data were interpolated on a 1 km regular grid. Two spectral ranges were defined, below and above 50 km. For scale below 50 km, the transects are subdivided in 100 km no-overlapping equal sections and multiplied with a Hamming window, that provides 56 late-winter and 70 summer subtransects. Above 50 km, the 700 km sections were not subdivided and only multiplied by Hamming window. Then Fourier transform is applied with the *pwelch* matlab® function that gives the mean spectra estimate and the 95% significance range using a chi-squared approach, which is reported in the figures (Figure 6). Note that in order to allow the comparison among power spectral density (PSD) of temperature, salinity, and seawater density, they are adimensionalized multiplying by $\alpha^2$, $\beta^2$, and $1/\rho_0{}^2$, respectively.

In addition to mesoscale and submesoscale motions of the thermohaline structures, TSG surveys can be influenced by high-frequency meteorological variability and upper ocean processes. Although the diurnal cycle of upper ocean temperature can reach in rare occasions more than 3°C, such large values are confined in the top meter of the upper ocean [*Gentemann et al.*, 2009]. During a winter intensive survey in the subtropical front of the Northern Pacific Ocean, *Hosegood et al.*, [2006] did not observe any large temperature diurnal cycle at 7 m depth. At the level of TSG measurements (3–5 m), the diurnal cycle is also likely to be small, with typical daily amplitudes on the order of 0.2°C. High-frequency meteorological events can also induce large changes in this latitude band. For example, *Hosegood et al.* [2006] observed a cooling reaching 2–3 degrees in a single day due to a winter storm. Furthermore, advection of mixed layer submesoscale fronts (with typical amplitudes of 3–5°C in this region) could induce a rapid change at the surface, with a displacement of typically 2 km in 6 h during a summer survey in the subtropical North Atlantic [*Reverdin et al.*, 2015]. Although the diurnal processes could be a moderate source of aliasing of TSG submesoscale measurements, 100 km subdivisions of the transect are nearly synoptic and crossed by the ships in 3–4 h, thus fast enough with respect to the daily cycle. We thus expect that diurnal processes or nonsynopticity have little influence on the scales between 5 and 50 km.

In QG theory, the Potential Energy (PE; ignoring the $^1/_2$ factor) is given by [*Wang et al.*, 2010]:

$$PE = \frac{1}{N^2}\langle b^2 \rangle \propto \langle \rho'^2 \rangle \tag{7}$$

where $N^2$ is the mean Brunt-Väisälä frequency, $b$ is the buoyancy ($=g\rho'/\rho_0$). $PE$ is proportional to the square of the seawater density fluctuations $\rho'$. To a first-order, the seawater density fluctuations are linearly dependent on temperature (T) and salinity (S) fluctuations following equation (1).

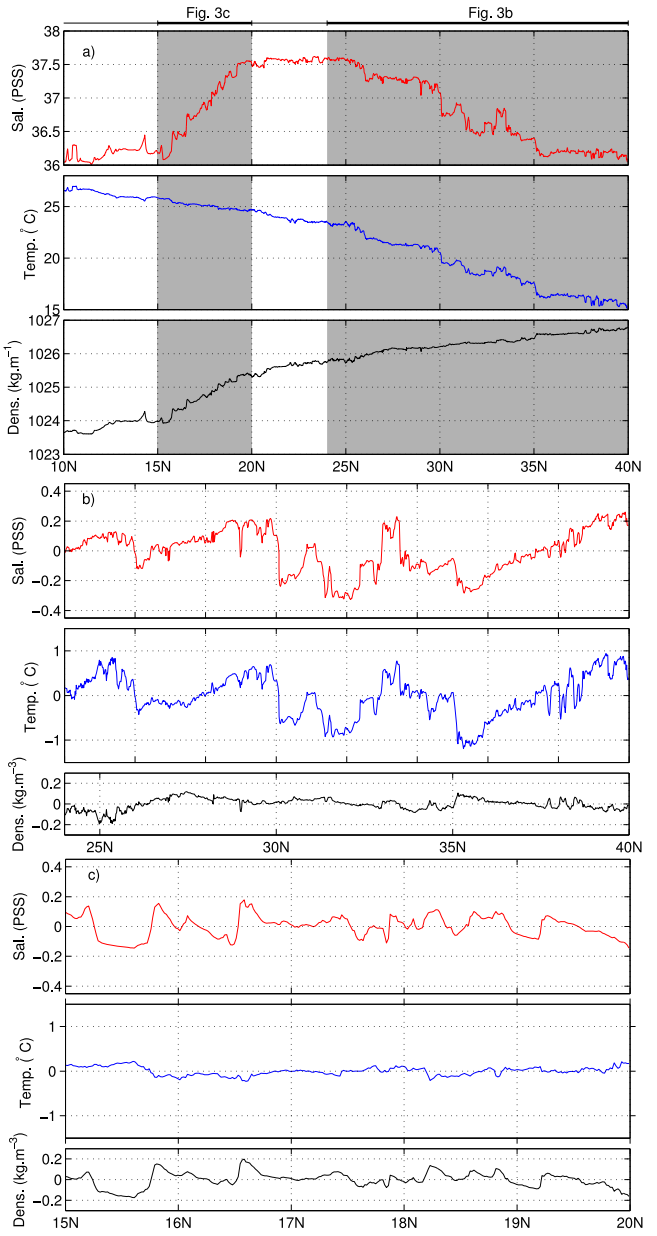


**Figure 3.** (a) Near surface salinity (red), temperature (blue), and density (black) measured along the MN *Colibri*'s TSG transect between 10° and 40°N during March 2011. (b) Near surface salinity, temperature, and density anomalies from the *Colibri*'s TSG transect and detrended between 24° and 40°N; (c) same as above, but between 15° and 20°N. Gray shading indicates the region of successive zooms along the latitude transect.

## 3. Thermohaline Variability in March 2011

The situation observed in March 2011 is well representative of the winter condition across the subtropical SSM. It is thus suited for illustrating the typical mesoscale and intraseasonal winter features. The Subtropical Atlantic is characterized by the SSM (up to 37.6 pss) located between 19° and 25°N, while the measured temperature shows a regular southward increase. The large-scale gradient of salinity (in absolute value) is stronger south of 19°N than north of 26°N.

We will first focus on the region located north of 24°N along the transect where the horizontal temperature and salinity gradients have the same sign, which can result in thermohaline compensation. The temperature, salinity, and density time series have been isolated between 24°N and 40°N (Figure 1), and then detrended (Figure 3b). They exhibit a high level of coherence (significant correlation coefficient of 0.92, significant at 95%), with a strong thermohaline front separating the warmer and saltier water from cooler and fresher waters, a feature that is particularly noticeable between 29° and 34°N.

On the south-western flank of the SSM between 15° and 20°N, the surface horizontal temperature and salinity gradients have opposite signs (Figures 1, 3a and 3c), thus contributing to increase the density gradient. The near-surface salinity and density show stronger variability at a scale of 50 km (Figure 3c, top and bottom), while the temperature shows relatively weak fluctuations at this scale (Figure 3c, middle). Contrary to the north-eastern (north of 24°N; Figure 1) part of the SSM, at all scales, the density fluctuations are mainly dominated by salinity fronts (Figure 3c).

In order to quantify the thermohaline fluctuation as a function of space and length scale, the wavelet transform of the T/S transects from the TSG have been performed. North of 34°N (Figure 4; dashed gray line), surface horizontal temperature and salinity fluctuations (described by wavelets) are in phase ($\Phi \sim 0°$; Figure 4b), and temperature fluctuations largely dominate ($|R| \geq 2$; Figure 4a) for 10–500 km wavelengths. Between 29° and 34°N and for 10–500 km wavelength, the density ratio values are mainly between 0.8 and 1.2 (Figure 4a; within dashed gray lines). This confirms the strong correlation between temperature and salinity

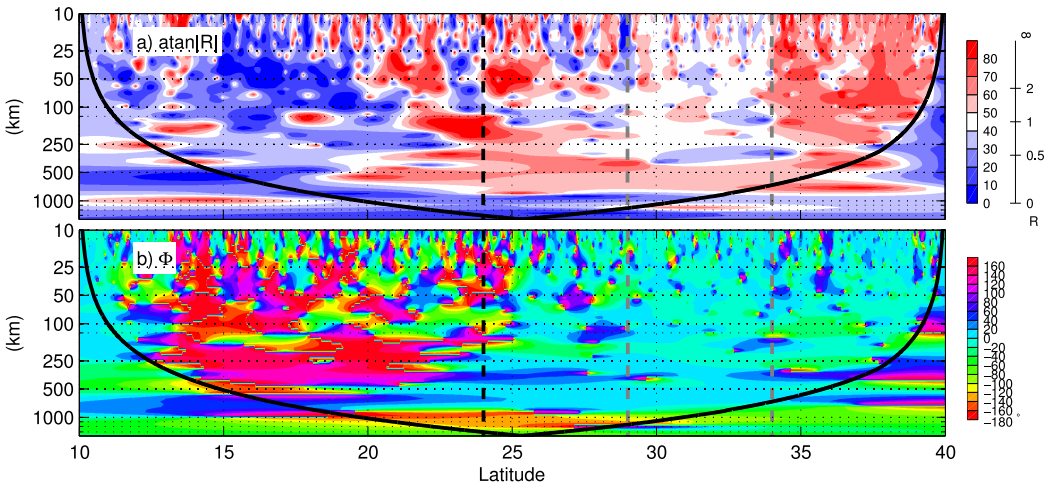


**Figure 4.** Norm (a) and phase (b) of the density ratio computed from the wavelet coefficients of temperature and salinity. The solid thick curve shows the cone of influence of the wavelet edge effects near 10°N and 40°N. Gray-dashed and black-dashed vertical lines define the latitudinal limits of the corresponding box in Figure 1.

variability, and weak density fluctuations observed in this region at every scale (Figures 3a and 3b). Furthermore, the fluctuations of temperature and salinity are also well in phase showing everywhere an angle of $\Phi \sim 0^\circ$ (Figure 4b). Thus, thermohaline compensation is observed at all 10–500 km wavelengths between 29° and 34°N.

At the latitude of the center of SSM (about 20°–24°N), at large-scale (>200km), the density ratio is not well defined due to the vanishing horizontal salinity gradient. At mesoscale and submesoscale, the density ratio presents both value greater than $|R|>2$ and lower than $|R|<0.5$, and $\Phi$ does not have a well-defined value (Figures 4a and 4b).

South of 20°N, the salinity fluctuation amplitude is stronger than the temperature one (Figures 3a and 3c), and density fluctuations are enhanced comparatively to the thermohaline ones (Figure 3c). This results in a density ratio lower than 0.6 for the 10–500 km wavelength (Figure 4a).We also note that at wavelengths between 200 and 500 km, temperature and salinity gradients are out-of-phase ($\Phi \sim 180^\circ$; Figure 4b). The south-western region of SSM is characterized by a strong northward gradient of salinity opposite to the southward gradient of temperature. In this region, the salinity acts to reinforce the surface horizontal gradient density at wavelengths between 200 and 500 km. At shorter wavelengths (<100km), the phase does not present a particular value (Figure 4b).

## 4. Seasonal Variability

### 4.1. Thermohaline Variability

In order to gain further insight into the seasonal variability of density ratio for horizontal scales between 5 and 200 km in the north-eastern SSM, the wavelet spectra for 19 TSG tracks from 2002 to 2011 between 40°N and 10°S are computed during February–March and August–September period. The Power Density Functions (PDF) of norm and angle of the complex density ratio given by wavelet analysis are computed within 24°–39°N region in the late winter density-compensated region (Figures 1 and 5) where the strongest seasonal variability of the density ratio was observed (not shown).

North of 24°N, during February–March, the seasonal PDF generalizes the individual thermohaline behavior observed for the March 2011 section within this latitudinal range. A striking result is that the PDF of the density ratio norm and mean angle are nearly constant ($|R| \sim 1$; $\Phi_R \sim 0^\circ$) for all wavelengths and the horizontal thermohaline structure is nearly compensated for all wavelengths in the range 5–200 km (Figures 5a and 5b). Note that, the compensation is better achieved at smaller scales than 25 km (Figures 5a and 5b).

In contrast, during August–September, between 24° and 39°N, the surface thermohaline gradients are not well compensated for wavelengths larger than 20 km. At these horizontal scales, the horizontal salinity

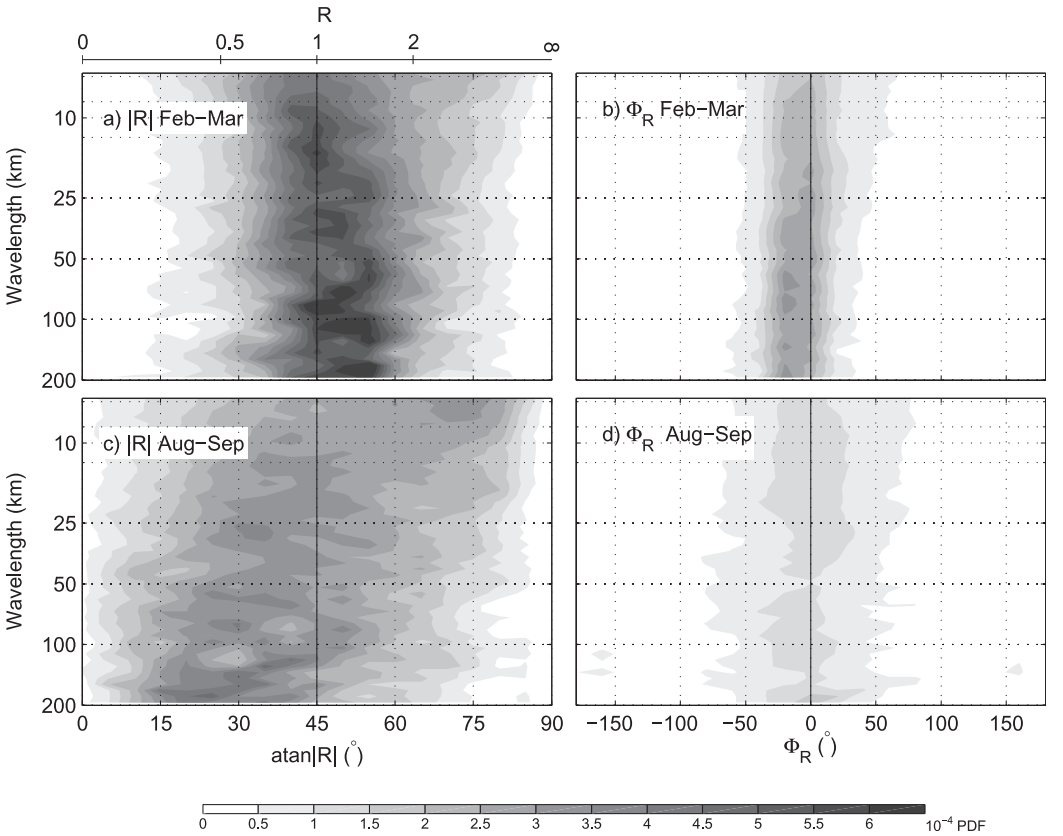


**Figure 5.** PDF of norm (a) and angle (b) of complex density ration as a function of length scale computed from wavelet coefficients of temperature and salinity for selected TSG transects between 24° and 39°N in February–March over the period 2002–2011. (c) and (d), same as Figures 5a and 5b, respectively, but for selected transects in August–September.

gradient dominates the density ratio with value around $|R|\sim 0.5$ (Figure 5c). The PDF of the norm and angle of the density ratio has a greater spread than during the winter season—especially at wavelengths smaller than 20 km—indicating a larger spatial and interannual variability, and uncertainty in density ratio estimates. During boreal summer, the atmospheric heating in the northern hemisphere and the large-scale currents contribute to shift the alignment away from $\Phi_R \sim 0^\circ$ and reduce the surface horizontal temperature gradient within 20–200 km scales, leading to a decrease of $|R|$ in the northern SSM (Figures 5c and 5d) [*Johnson et al*., 2012].

### 4.2. Themohaline Spectra

In order to examine the impact of the thermohaline horizontal variability on horizontal density variability and the potential energy distribution, the temperature, salinity, and density power spectral density estimates were computed with associated confidence level at 95% (Figure 6) during late winter and summer between 29° and 34°N, in the region of late winter density compensation of the Subtropical Azores Current/Front (Figure 2). During late boreal winter, between 20–100 km the temperature and salinity spectra present a slope in $k^{-2}$, while for longer wavelengths, a $k^{-1}$ slope appears, in spite of a larger uncertainty (thick black lines, Figure 6a). At wavelengths under 20 km, temperature and salinity are associated with a $k^{-3}$ slope. Because horizontal density compensation often occurs during this season, the density fluctuations are 4 times less energetic than both its temperature and salinity components, which may behave like passive tracers and conserve sharp temperature and salinity fronts characterized by spectral $k^{-2}$ slope at scales between 20 and 100 km (Figure 6a). In contrast, the density spectra present a steeper $k^{-3}$ slope between 5 and 50 km, except for a plateau at $k^{-1}$ between 20 and 35 km (Figure 6a). However, this plateau could have resulted from a differences between the averaged transects. Indeed, while under 20–50 km wavelength individual density spectra present a clear a $k^{-3}$ slopes, above these scales, the slope presents a larger range of variability (not shown) resulting in a flatter density spectra mean slope around $k^{-2}$. Above

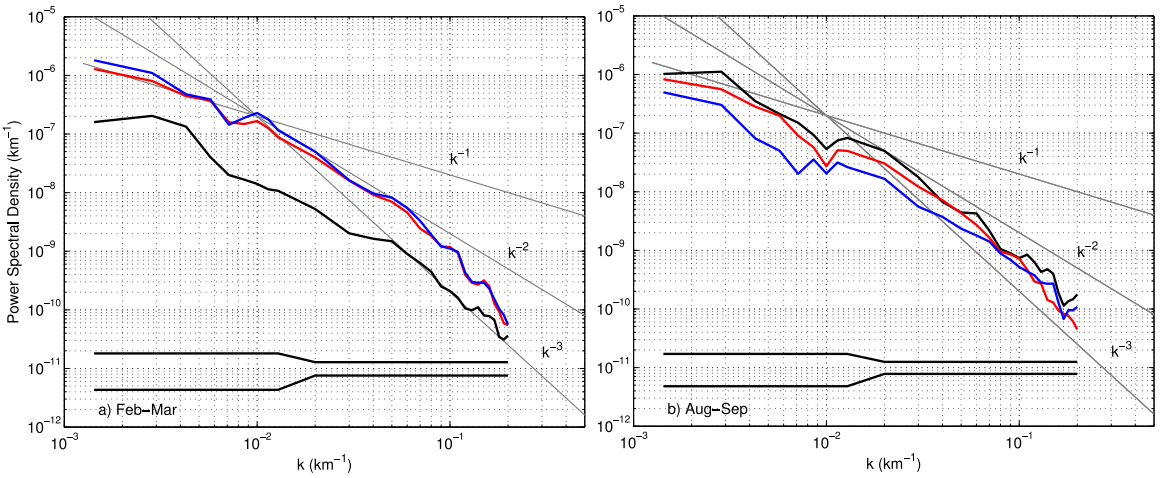


**Figure 6.** (a) A dimensional temperature (blue), salinity (red), and density (black) power spectral density computed from TSG transects between 29° and 34°N in February–March over the period 2002–2011. $k^{-1}$, $k^{-2}$, and $k^{-3}$ spectral slopes are indicated in gray line. Thick horizontal black lines show 95% confidence interval (see text). (b) Same as Figure 6a but in August–September.

150 km length-scale, a broad peak is found in density spectra, probably related to the scales associated with the Azores front and eddies (150–200 km) observed in the region [*Alves and Colin de Verdière*, 1999; *Chelton et al.*, 2007; *Tulloch et al.*, 2011].

During summer, for scales of 5–100 km, the energy level of temperature and salinity has diminished, while density energy has strongly increased by nearly 4 times over late winter values. This confirms that the

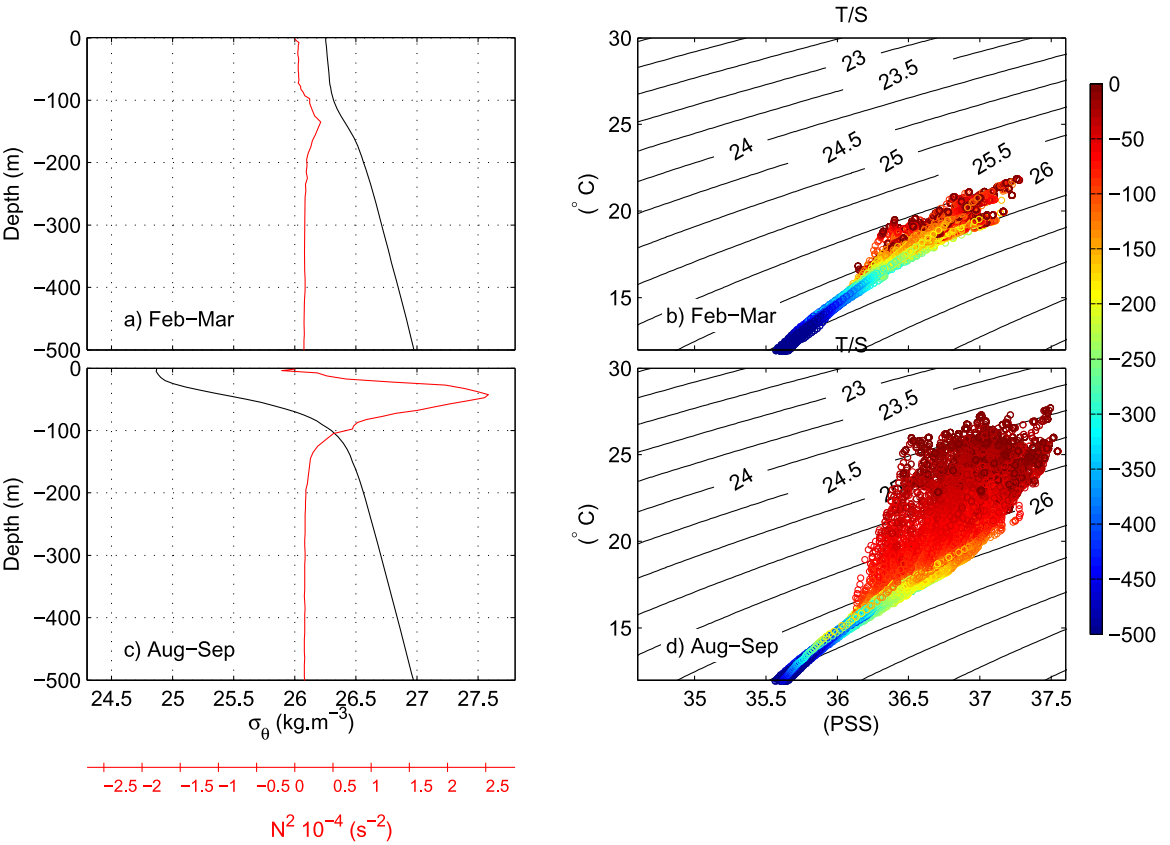


**Figure 7.** (a) Mean density (black) and Brunt-Väisälä frequency (red) profiles between 0 and 500 m depth; (b) T-S diagram computed from Argo profiles available in February–March over the period 2004–2012 within the gray box of Figure 1. Colors indicate the depth range. (c) and (d), same as Figures 7a and 7b, respectively, but in August–September.

salinity and temperature fluctuations act constructively to enhance the density fluctuations, with a major contribution of salinity fluctuations above 10 km wavelength (Figure 6b). In contrast with winter season, the temperature, salinity, and density summer spectra all present a flatter slope around $k^{-3}$–$k^{-2}$ ($k^{-2}$–$k^{-1}$) between 10 and 50 km (above 50 km) (Figure 6b). However, salinity summer spectra exhibit a steeper slope below 10 km.

### 4.3. Thermohaline Vertical Structure

In order to better understand the vertical context of density compensation and turbulent potential energy spectra, the T-S diagrams are examined as well as the mean density and associated Brunt-Väisälä profiles in the upper 500 m ocean layer (Figure 7) of the box 35°–25°W/29°–34°N between 2004 and 2012. The boreal winter profiles indicate a deep well-mixed layer on the order of 150 m depth overlying a nearly constant stratification (Figure 7a). The density range of the mixed layer waters are comparable to the permanent pycnocline ones $\sigma\theta$=26–26.6 kg.m$^{-3}$ (Figure 7b). This suggests that the thermohaline properties and associated dynamics observed at the surface may reflect more interior dynamics since the winter density and stratification are not intensified near the surface. Indeed, this area is located across the 1000 m deep Azores Current which is strongly baroclinically unstable, and could affect the dynamics of the region in terms of QG turbulent cascade [*Alves and Colin de Verdière*, 1999].

On the other hand, the summer density and stratification profiles show a sharp seasonal pycnocline ($N^2$=2.5 $10^{-5}$ $s^{-2}$ at 50 m depth, Figure 7c) associated with a very shallow mixed layer, explained by the large-scale and relatively uniform summer solar heating which reduces the meridional SST gradient, but leaves the SSS meridional gradient unchanged, hence the near surface scatter in T-S diagram (Figure 7d) [*Johnson et al*., 2012; *Kolodziejczyk et al*., 2015]. This is confirmed by the low level of temperature energy at scales $>\sim$20 km. In contrast, the salinity fluctuations associated with the Azores Current/Front instabilities [*Kolodziejczyk et al*., 2015] maintain a high level of density energy. Below 20 km, the flatter slope temperature and density spectra during summer could result from the submesoscale dynamics and ageostrophic mixed-layer dynamics likely at works in the summer mixed layer (i.e., frontogenesis, front advection, Ekman currents, internal waves or near-inertial waves) [*Callies and Ferrari*, 2013].

## 5. Discussion and Conclusions

The analysis of surface mesoscale and submesoscale horizontal thermohaline structures in the subtropical SSM reveals very different spatiotemporal patterns. In the north-eastern SSM (north of 25°N and east of 40°W), during late boreal winter, the thermohaline compensation is found at all scales from 5 to 500 km. This result is corroborated by studies in comparable regions of the Pacific ocean [e.g., *Samelson and Paulson*, 1988; *Ferrari and Rudnick*, 2000; *Cole et al*., 2010] and North Atlantic Oceans [*Rudnick and Martin*, 2002]. The observed horizontal compensation is associated with strong vertical mixing, as suggested by deep late-winter mixed layer, which is ubiquitous in the eastern subtropical regions under winter cooling and destabilizing salinity vertical gradient within the upper ocean [e.g., *Yeager and Large*, 2007; *Cole et al*., 2010; *Kolodziejczyk and Gaillard*, 2013].

The thermohaline compensation explains the more energetic spectra of temperature and salinity in comparison to the density spectra. Above 100 km scales—the synoptic scales of mesoscale eddies and fronts in the baroclinically unstable Azores current regions [e.g. *Alves and Colin de Verdière*, 1999; *Juliano and Alves*, 2007; *Chelton et al*., 2007; *Tulloch et al*., 2011; *Kolodziejczyk et al*., 2015]—in spite of a larger uncertainty, the temperature, and salinity spectra exhibit a $k^{-1}$ slope compatible with the spectral slope of passive tracer in interior QG turbulence theory [*Charney*, 1971; *Callies and Ferrari*, 2013]. This is expected, due to the tracer-like behavior of horizontal density compensated temperature and salinity [*Klein et al*., 1998; *Smith and Ferrari*, 2009; *Callies and Ferrari*, 2013]. However, in this range of length scale the flattening of temperature and salinity spectra may also be associated with the signature of the Azores thermohaline front and mesoscale eddies [*Kolodziecjzyk et al*., 2015], as suggested by the broad peaks of the density spectra around 500–150 km [*Klein et al*., 2008].

At scales between 20 and 100 km, temperature and salinity spectra have a characteristic slope in $k^{-2}$ for successive series of sharp thermohaline fronts, due to stirring of thermohaline compensated fronts while the density fronts are rapidly slumped and mixed [e.g., *Young*, 1994; *Klein et al*., 1998; *Marshall and Schott*,

1999; *Rudnick and Ferrari*, 1999; *Ferrari and Rudnick*, 2000; *Rudnick and Martin*, 2002; *Ferrari and Paparella*, 2003; *Cole et al*., 2010]. Surprisingly, in the range 50–100 km scales, density spectra also exhibit a near $k^{-2}$ slope much flatter than what would be expected in the case of thermohaline compensation [e.g., *Klein et al*., 1998; *Smith and Ferrari*, 2009]. This may be explained by the nonfull compensation that may occur in the data set, which leaves lower-amplitude frontal density features (Figure 3b). This can be also related to spatial inhomogeneity of the horizontal thermohaline compensation over the winter mixed layer due to stochastic atmospheric forcing or ageostrophic dynamics [*Ferrari and Rudnick*, 2000; *Klein et al*., 2008; *Capet et al*., 2008; *Callies and Ferrari*, 2013]. Interannual averaging of the thermohaline spectra may also flatten the spectra because of year-to-years and spatial variability of the compensated structures distribution. This could also explain the density spectra flatter plateau between 20 and 50 km.

At wavelengths smaller than 20 km, the thermohaline variability is also more energetic than the density variability, but both drop off with slopes not flatter than $k^{-3}$. It suggests that small-scale features of tracers are associated with interior QG turbulence structures [*Charney*, 1971; *Klein et al*. 1998; *Callies and Ferrari*, 2013], and departing from flatter spectra expected by previous observational results in a similar region [*Ferrari and Rudnick;* 2000; *Hodges and Rudnick*, 2006; *Callies and Ferrari;* 2013]. By comparison, in the Subtropical Front in the Northern Pacific*, Samelson and Paulson* [1988] found similar results, except that the $k^{-3}$ slope of the temperature spectra computed within 156°–150°W/26°–34°N is found under 10 km wavelength. In contrast, further east close to the Northern Subtropical Pacific front along 140°W, during the same season (January–February), *Hodges and Rudnick* [2006] found an invariable potential temperature spectra in $k^{-2}$ between 1 and 100km wavelength, while *Callies and Ferrari* [2013] found a potential energy spectral slope between $k^{-2}$ and $k^{-3}$ (their Figure 6). An explanation for this difference between spectra slopes at 140°W and west of 150°W in the Pacific Ocean is associated with the presence, in the latter region, of the eastern tail of the Eastern Subtropical Pacific Front and associated current (*Roden*, 1980; *Lynn*, 1986; *Kobashi et al*., 2006, *Qiu et al*., 2008]. This current could be baroclinically unstable and the potential energy spectra compatible with interior QG turbulence [*Roden*, 1980, 1981; *Samelson and Paulson*, 1988; *Wang et al*., 2010]. Further east, along 140°W, the region is less influenced by current instabilities, but could be subject to mixed layer instability and frontal advection at the surface [*Young*, 1994, *Rudnick and Ferrari*, 1999; *Boccaletti et al*., 2007; *Capet et al*., 2008; *Cole et al*., 2010]. In the present study, we suggest that vertical mixing can also be intensified during winter, destroying thermohaline features at small scale [e.g., *Yeager and Large*, 2007; *Cole et al*., 2010; *Kolodziejczyk and Gaillard*, 2013]. However, this spectral drop off could be an artifact associated to sampling [*Capet et al*., 2008; *Callies and Ferrari*, 2013].

During boreal summer, the compensation does not hold at large to submesoscales, likely due to summer heating and reduced vertical mixing of the upper ocean [*Johnson et al*., 2012; *Cole et al*., 2010; *Kolodziejczyk et al*., 2015]. In contrast to the winter situation, during late summer in the north-eastern SSM, the density spectra are more energetic, while temperature and salinity spectra are less energetic. This is primary explained by the noncompensated temperature and salinity horizontal structures. At scales larger than 10 km, the salinity spectra are more energetic than the temperature spectra which confirm the role of salinity in controlling the density fluctuation during summer [*Kolodziejczyk et al*., 2015]. The spectra are also flatter (steeper) with slopes closer to $k^{-2}$ at scales below (above) 50 km, but not significantly distinguishable from $k^{-3}$ ($k^{-1}$) because of the error bars.

Given the mixed layer vertical thermohaline structure, the local mixed layer Rossby radius of deformation is of the order of $\sim$ 1–10 km [*Rudnick and Martin*, 2002]. Thus especially for scale below 10 km, the mixed layer dynamic could be enhanced [*Boccaletti et al*., 2007; *Capet et al*., 2008]. In contrast with winter season, this suggests that mixed layer ageostrophic dynamics of the summer mixed layer partially mask the interior QG regime [*Klein et al*., 2008], due to different near surface stratification which possibly isolates the mixed layer dynamics from the interior regime. This ageostrophic signature may be due to a different mechanisms: e.g., frontal advection, Ekman flow, near-inertial waves/tides [*Callies and Ferrari*, 2013], or diurnal variability. However, with the present data set, it is difficult to pin-point the main mechanism.

Unfortunately, the along tracks vessels data do not provide surface horizontal current and deeper thermohaline measurements. To get more insight into surface horizontal turbulence regime, estimation of kinetic energy and vertical structure of the energy spectra is mandatory. Nevertheless, here it is suggested that the seasonal variability of atmospheric flux, through its impact on the upper ocean stratification, has a strong impact on the small scale horizontal surface turbulent potential energy distribution. This study also shows

the potential of the large and unique available TSG data base (http://www.legos.obs-mip.fr/observation/sss/) for studying mesoscale and submesoscale surface thermohaline variability over most of the global ocean regions.

**Acknowledgments**

N. Kolodziejczyk is supported by a CNES (French National Space Agency) post-doctoral grant. Sea Surface Salinity data derived from thermosalinograph instruments installed onboard "MN *Toucan*" and "MN *Colibri*" voluntary observing ships were collected, validated, archived, and made freely available by the French Sea Surface Salinity Observation Service (SO-SSS; http://www.legos.obs-mip.fr/observation/sss/). The Argo profiles have been downloaded from Coriolis Argo GDAC (http://www.coriolis.eu.org/Data-Services-Products/View-Download). The MODIS SST images were downloaded from http://oceancolor.gsfc.nasa.gov/. The authors acknowledge the MODIS and Oceancolor NASA projects for providing freely the MODIS SST map. The authors wish to thank Claire Menesguen and Aurélien Ponte for valuable discussions about this paper, and Christopher W. Brown for useful corrections and comments on this manuscript. The authors also thank two anonymous reviewers for their valuable comments and suggestions which improved substantially the manuscript.

## References

Alves J. L.G. R., and A. Colin de Verdière (1999), Instability dynamics of a subtropical jet and applications to the Azores front current system: Eddy-driven mean flow, *J. Phys. Oceanogr.*, *29*, 832–864.

Boccaletti, G., R. Ferrari, and B. Fox-Kemper (2007), Mixed layer instability and restratification, *J. Phys. Oceanogr.*, *37*, 2228–2250.

Boutin, J., P. Waldteufel, N. Martin, G. Caudal, and E. Dinnat (2004), Surface salinity retrieved from SMOS measurements over the global ocean: Imprecisions due to sea surface roughness and temperature uncertainties, *J. Atmos. Oceanic Technol.*, *21*, 1432–1447, doi: 10.1175/1520-0426(2004)021<1432:ssrfsm>2.0.CO;2.

Callies, J., and R. Ferrari, (2013), Interpreting energy and tracer spectra of upper-ocean turbulence in the submesoscale range (1–200 km), *J. Phys. Oceanogr.*, *43*, 2456–2474, doi:10.1175/JPO-D-13-063.1.

Capet, X., J. C. McWilliams, M. J. Molemaker, and A. F. Shchepetkin, (2008), Mesoscale to submesoscale transition in the California current system. Part I: Flow structure, eddy flux, and observational tests. *J. Phys. Oceanogr.*, *38*, 29–43.

Charney, J. G. (1971), Geostrophic turbulence, *J. Atmos. Sci.*, *28*, 1087–1095.

Chelton, D. B., M. G. Schlax, R. M. Samelson, and R. A. de Szoeke (2007), Global observation of large Oceanic eddies, *Geophys. Res. Lett.*, *34*, L15606, doi:10.1029/2007GL030812.

Cole, S. T., D. L. Rudnick, and J. A. Colosi (2010), Seasonal evolution of upper-ocean horizontal structure and the remnant mixed layer, *J. Geophys. Res.*, *115*, C04012, doi:10.1029/2009JC005654.

Dong, C., J. C. McWilliams, Y. Liu, and D. Chen (2014), Global heat and salt transports by eddy movement, *Nat. Commun.*, *5*, 1–5, doi: 10.1038/ncomms4294.

Ferrari, R., and D. L. Rudnick (2000), Thermohaline varaibility in the upper ocean, *J. Geophys. Res.*, *105*, 16,857–16,883, doi:10.1029/2000JC900057.

Ferrari, R., and F. Paparella (2003), Compensation and Alignment of Thermohaline Gradients in the Ocean Mixed Layer, *J. Phys. Oceanogr.*, *33*, 2214–2223, doi:10.1175/1520-0485(2003)0332.0.CO;2.

Font, J., A. Camps, A. Borges, M. Martin-Neira, J. Boutin, N. Reul, Y. H. Kerr, A. Hahne, and S. Mecklenburg, (2010), SMOS: The challenging sea surface salinity measurement from space, *Proc. IEEE*, *98*(5), 649–665 doi:10.1109/JPROC.2009.2033096.

Fox-Kemper, B., and R. Ferrari (2008), Parametrization of the mixed layer eddies. Part I: Prognostic and impact, *J. Phys. Oceanogr.*, *38*(6), 1166–1179.

Fox-Kemper, B., R. Ferrari, and R. Halberg (2008), Parametrization of the mixed layer eddies. Part I: Theory and diagnosis, *J. Phys. Oceanogr.*, *38*(6), 1145–1165.

Gentemann, C. L., P. J. Minnett, and B. Ward (2009), Profiles of ocean surface heating (POSH): A new model of upper-ocean diurnal warming, *J. Geophys. Res.*, *114*, C07017, doi:10.1029/2008JC004825.

Haine, T. W. N., and J. Marshall (1998), Gravitational, symmetric and baroclinic instability of the ocean mixed layer, *J. Phys. Oceanogr.*, *28*, 634–658.

Hernandez, O., J. Boutin, N. Kolodziejczyk, G. Reverdin, N. Martin, F. Gaillard, N. Reul, and J.-L. Vergely, (2014), SMOS salinity in the subtropical north Atlantic salinity maximum. Part I: Comparison with aquarius and in situ salinity, *J. Geophys. Res. Oceans*, *119*, 8878–8896, doi: 10.1002/2013JC009610.

Hodges, B. A., and D. L. Rudnick, (2006), Horizontal variability in chlorophyll fluorescence and potential temperature, *Deep Sea Res., Part I*, *53*, 1460–1482, doi:10.1016/j.dsr.2006.06.006.

Hosegood, P. J., M. C. Gregg, and M. H. Alford (2006), Sub-mesoscale lateral density structure in the oceanic surface mixed layer, *Geophys. Res. Lett.*, *33*, L22604, doi:10.1029/2006GL026797.

Johnson, G. C., S. Schimidtko, and J. M. Lyman (2012), Relative contributions of temperature and salinity to seasonal mixed layer density changes and horizontal density gradient, *J. Geophys. Res.*, *117*, C04015, doi:10.1029/2011JC007651.

Juliano, F. M., and M. L. G. R. Alves (2007), The Atlantic subtropical front/current systems of Azores and St. Helena, *J. Phys. Oceanogr.*, *37*, 2573–2598, doi:10.1175/2007JPO3150.1.

Klein, P., A.-M. Treguier, and B. L. Hua (1998), Three-dimensional stirring of the thermohaline front, *J. Mar. Res.*, *56*, 589–612.

Klein, P., B. L. Hua, G. Lapeyre, X. Capet, S. Le Gentil, and H. Sasaki (2008), Upper-ocean turbulence from high-resolution 3D simulations, *J. Phys. Oceanogr.*, *38*, 1748–1763.

Kobashi, F., H. Mitsudera, and S.-P. Xie (2006), Three subtropical fronts in the North Pacific: Observational evidence for mode water-induced subsurface frontogenesis, *J. Geophys. Res.*, *111*, C09033, doi:10.1029/2006JC003479.

Kolodziejczyk, N., and F. Gaillard (2013), Variability of the heat and salt budget in the subtropical South-Eastern Pacific mixed layer between 2004 and 2010: Spice injection mechanism, *J. Phys. Oceanogr.*, *43*, 1880–1898.

Kolodziejczyk, N., O. Hernandez, J. Boutin, and G. Reverdin (2015), SMOS salinity in the subtropical north Atlantic salinity maximum. Part II: Horizontal thermohaline variability, *J. Geophys. Res. Oceans*, *120*, 972–987, doi:10.1002/2014JC010103.

Kolodziejczyk, N., O. Hernandez, J. Boutin, and G. Reverdin (2015), SMOS salinity in the subtropical north Atlantic salinity maximum. Part II: 503. Horizontal thermohaline variability, *J. Geophys. Res. Oceans*, *120*, 972–987, doi:10.1002/2014JC010103.

Lynn, R. J. (1986), The subarctic and the northern subtropical fronts in the eastern north Pacific ocean spring, *J. Phys. Oceanogr.*, *16*, 209–222.

Marshall, J., and F. Scott (1999), Open-ocean convection: Observations, theory and models, *Rev. Geophys.*, *37*(1), 1–64.

Mignot, J., A. Lazar, and M. Lacarra (2012), On the formation of barrier layers and associated vertical temperature inversions: A focus on the northwestern tropical Atlantic, *J. Geophys. Res.*, *117*, C02010, doi:10.1029/2011JC007435.

Qiu, B., R. B. Scot and S. Chen (2008), Length scale of eddy generation and nonlinear evolution of the seasonally modulated South Pacific Subtropical Countercurrent, *J. Phys. Oceanogr.*, *38*, 1515–1528.

Reul, N, J. Tenerelli, J. Boutin, B. Chapron, F. Paul, E. Brion, F. Gaillard, and O. Archer (2012), Overview of the first SMOS sea surface salinity products. Part I: Quality assessment for the second half of 2010, *IEEE Trans. Geogr. Remote Sens.*, *50*(5), 1636–1647, doi:10.1109/TGRS.2012.2188408.

Reul, N., et al. (2013), Sea surface salinity observations from space with the SMOS satellite: A new means to monitor the marine branch of the water cycle, *Surv. Geophys.*, *35*, 1–42, doi:10.007/s10712-013-9244-0.

Reverdin, G., E. Kestenare, C. Franckignoul, and T. Delcroix (2007), Surface salinity in the Atlantic ocean (30°S–50°N), *Prog. Oceanogr.*, *73*, 311–340.
Reverdin, G., et al. (2015), Surface salinity in the North Atlantic subtropical gyre during the STRASSE/SPURS summer 2012 cruise, *Oceanography*, *28*(1), 84–93, doi:10.5670/oceanog.2015.09.
Roden, G., I (1974), Thermohaline structure, fronts and sea-air energy exchange of the trade wind region east of Hawaii, *J. Phys. Oceanogr.*, *4*, 168–182, doi:10.1175/1520-0485(1974)004<0168:TSFASA>2.0.CO;2.
Roden, G. I. (1980), On the subtropical frontal zone north of Hawaii during winter, *J. Phys. Oceanogr.*, *10*, 342–363.
Roden, G. I. (1981), Mesoscale thermohaline, sound velocity and Baroclinic flow structure of the Pacific subtropical front during the winter of 1980. *J. Phys. Oceanogr.*, *11*, 658–675, doi:10.1175/1520-0485(1981)011<0658:MTSVAB>2.0.CO;2.
Roden, G. I. (1991), Mesoscale flow and thermocline structure around Fieberling seamount, *J. Geophys. Res.*, *96*, 16,653–16,672, doi:10.1029/91JC01747.
Rudnick, D. L., and R. Ferrari (1999), Compensation of the horizontal temperature and salinity gradient in the ocean mixed layer, *Science*, *283*, 526–529.
Rudnick, D. L., and J. P. Martin (2002), On the horizontal density ratio in the upper ocean, *Dyn. Atmos. Oceans*, *36*, 3–21.
Rudnick, D. L., and J. R. Luyten (1996), Intensive surveys of the Azores Front: 1. Tracers and dynamics, *J. Geophys. Res.*, *101*(C1), 923–939, doi:10.1029/95JC02867.
Samelson, R. M., and C. A. Paulson (1988), Towed thermistor chain observations of fronts in the subtropical north Pacific, *J. Geophys. Res.*, *93*, 2237–2246, doi:10.1029/JC093iC03p02237.
Smith K. S., and R. Ferrari (2009), The production and dissipation of compensated thermohaline variance by mesoscale stirring, *J. Phys. Oceanogr.*, *39*, 2477–2501.
Stommel, H. M. (1993), A conjectural regulating mechanism for determining the thermohaline structure in the ocean mixed layer, *J. Phys. Oceanogr.*, *23*, 142–148.
Tailleux, R., A. Lazar, and C. J. C. Reason (2005), Physics and Dynamics of Density-Compensated Temperature and Salinity Anomalies. Part I: Theory, *J. Phys. Oceanogr.*, *35*, 849–864. doi:10.1175/JPO2706.
Tanguy, Y., S. Arnault, and P. Lattes (2010), Isothermal, mixed layers and barriers layers in the tropical and sub-tropical Atlantic ocean during the ARAMIS experiment, *Deep Sea Res*. I, doi:10.1016/j.dsr.2009.12.012.
Torrence, C., and G. P. Compo (1998), A practical guide to wavelet analysis, *Bull. Am. Meteorol. Soc.*, *79*(1), 61–78.
Tulloch, R., J. Marshall, C. Hill, and K. S. Smith (2011), Scales, growth, and Spectral fluxes of baroclinic instability in the Ocean, *J. Phys. Oceanogr.*, *41*, 1057–1076. doi:10.1175/2011JPO4404.1.
Wang, D.-P., C. N. Flagg, K. Donohue, and H. T. Rossby, (2010), Wavenumber spectrum in the Gulf Stream from shipboard ADCP observations and comparison with altimetry measurements, *J. Phys. Oceanogr.*, *40*, 840–844.
Yeager, G. S., and W. G. Large (2007), Observational evidence of winter spice injection, *J. Phys. Oceanogr.*, *37*, 2895–2019.
Young, W. R. (1994), The subinertial mixed layer appriximation, *J. Phys. Oceanogr.*, *24*, 1812–1826.

## Erratum

In the originally published version of this article, equation 7 was printed with a typographical error, and was missing the proportional symbol ($\propto$). This error has since been corrected and this version may be considered the authoritative version of record.